NASA Technical Memorandum 87707 NASA-TM-87707 19860015186

UNSTEADY TRANSONIC FLOW CALCULATIONS FOR WING-FUSELAGE CONFIGURATIONS

JOHN T. BATINA

MARCH 1986

National Aeronautics and Space Administration

Langley Research Center
Hampton, Virginia 23665

UNSTEADY TRANSONIC FLOW CALCULATIONS FOR WING-FUSELAGE CONFIGURATIONS

John T. Batina
NASA Langley Research Center
Hampton, Virginia 23665-5225

Abstract

Unsteady transonic flow calculations are presented for wing-fuselage configurations. Calculations are performed by extending the XTRAN3S (Version 1.5) unsteady transonic small-disturbance code to allow the treatment of a fuselage. The research was conducted as part of a larger effort directed toward developing the capability to treat a complete flight vehicle. Details of the XTRAN3S fuselage modeling are discussed in the context of the small-disturbance equation. Transonic calculations are presented for three wing-fuselage configurations with leading edge sweep angles ranging from 0° to 46.76°, the results of which compare well with available experimental steady pressure data. Unsteady calculations are performed for simple bending and torsion modal oscillations of the wing. Comparisons of sectional lift and moment coefficients for the wing-alone and wing-fuselage cases reveal effects of fuselage aerodynamic interference on the unsteady wing loading. Tabulated generalized aerodynamic forces typically used in flutter analyses, indicate small changes in the real (in-phase) component and as much as a 30% change in the imaginary (out-of-phase) component when the fuselage is included in the calculation. These changes result in a 2 to 5% increase in total magnitude and a several degree increase in phase.

Nomenclature

A_{ij}	generalized aerodynamic force resulting from pressure induced by mode j acting through displacements of mode i
AR	full-span aspect ratio
c	airfoil chord
c_ℓ	sectional lift coefficient
c_m	sectional pitching moment coefficient about local midchord
c_r	wing reference chord
C_p	pressure coefficient
C_p^*	critical pressure coefficient
f	function defining instantaneous position of wing
F	function defining instantaneous position of fuselage
F	fuselage fineness ratio
k	reduced frequency, $\omega c_r/2U$
L	fuselage length
M	freestream Mach number
n	unit vector outward normal to surface of fuselage
TR	taper ratio
t	time, nondimensionalized by freestream velocity and wing reference chord
U	freestream velocity
x,y,z	nondimensional Cartesian coordinates in streamwise, spanwise, and vertical directions, respectively
α	angle of attack
γ	ratio of specific heats
Δt	nondimensional time step
Λ	sweep angle of wing leading edge
$\bar{\eta}$	fractional semispan
ξ,η,ζ	transformed nondimensional coordinates in x, y, and z directions, respectively
ϕ	disturbance velocity potential
ω	angular frequency

Subscripts

comp	computational
F	fuselage
J	index of grid points in spanwise direction
J_S	index of grid point adjacent to side boundary of computational fuselage surface (see Fig. 2(a))
k	index of grid points in vertical direction
k_b	index of grid point just below bottom boundary of computational fuselage surface (see Fig. 2(a))
k_t	index of grid point just above top boundary of computational fuselage surface (see Fig. 2(a))
W	wing

Introduction

Computational methods for predicting flow fields about wing-fuselage and multiple component configurations have been developed over recent years (see Refs. 1-9, for example). Techniques based on the doublet lattice method and the method of images have been reported by Giesing, Kalman, and Rodden[1] for calculating steady and oscillatory aerodynamics for interfering wings and bodies. Computer programs based on panel methods such as that developed by Woodward,[2,3] may be used for analyzing wing-body-tail configurations. More recently, computer programs such as PANAIR[4] have been developed for the analysis of complete flight vehicles. The underlying linear theory on which these methods are based, though, restricts the applications to subsonic and supersonic flows.

At transonic speeds, finite-difference methods are generally employed for the computation of transonic flows about wing-fuselage configurations. In the context of the transonic small-disturbance (TSD) equation, for example, Bailey and Ballhaus[5] calculated the transonic flow about nonlifting wing-cylinder combinations using a relaxation method. Steady pressure distributions were presented for a 30° swept wing on straight and area-ruled cylinders. Klunker and Newman[6] reported steady pressure results for a lifting wing centrally mounted on a cylindrical body. A coordinate transformation

simplified the fuselage flow-tangency boundary condition and line relaxation was used to solve the TSD equation. Bailey and Ballhaus[7] continued their work of Ref. 5 to treat nonlifting wings mounted on finite length fuselages. The computed results compared well with experimental data for both rectangular and swept wing-fuselage configurations at transonic Mach numbers. Boppe[8] extended these relaxation methods to compute transonic flows about realistic wing-fuselage configurations using a grid embedding technique. The method can treat configurations with arbitrary fuselage shapes since details of the flow are resolved using a locally embedded fine grid. In Ref. 8, steady transonic calculations for several wing-fuselage configurations showed excellent agreement with experimental data. Boppe and Stern[9] have extended the method of Ref. 8 to treat fairly complex aircraft configurations by including nacelles, pylons, and winglets in the analysis.

Although the finite-difference methods based on the TSD equation are applicable to transonic wing-fuselage cases, the solution techniques are restricted to steady flows. Solutions for unsteady transonic flow fields have recently been made possible using computer codes such as XTRAN3S.[10] The XTRAN3S unsteady TSD code was developed by the Boeing Military Airplane Company (BMAC) under USAF contract and is the most fully developed U.S. code for transonic aeroelastic analysis of isolated planar wings. Because of the need to be able to perform aeroelastic analyses for complete aircraft configurations, XTRAN3S is being modified to enable treatment of the additional aircraft components such as the fuselage, canard, tail, pylons, nacelles, stores, and control surfaces. These modifications to XTRAN3S are being developed under a cooperative agreement between AFWAL, NASA/Langley, NASA/Ames, and BMAC. The capability to treat multiple lifting surface configurations such as closely-coupled canard-wing and wing-tail geometries has already been developed and reported by the author.[11] A wing-tip store modeling capability has also recently been implemented by Guruswamy, Goorjian, and Tu.[12]

The purpose of the present paper is to present the development of the XTRAN3S wing-fuselage capability for predicting transonic unsteady aerodynamic loads for aeroelastic applications. The objectives of the research were to (1) modify the XTRAN3S code to allow the treatment of a fuselage; (2) validate the method by making comparisons with available experimental data, and (3) investigate and demonstrate the effects of fuselage aerodynamic interference on transonic pressures and forces on the wing. In this study steady calculations were performed for three wing-fuselage configurations to assess the fuselage treatment by making comparisons with experimental data. Unsteady calculations were performed for a transport-type wing-fuselage to demonstrate application to aeroelastic problems. The paper presents a detailed description of the XTRAN3S wing-fuselage modeling along with the results and comparisons which assess the new capability.

Computational Procedures

In this section, Version 1.5[13] of the XTRAN3S transonic code is briefly described. A detailed discussion of fuselage modeling and the development of the XTRAN3S wing-fuselage capability are also given.

XTRAN3S Transonic Code

The XTRAN3S code provides a time-accurate finite-difference solution to the nonlinear, small-disturbance, potential equation for transonic flow. The code can be used to calculate steady and unsteady transonic flow fields about planar wings including aeroelastic deformation effects. The program is capable of treating either forced harmonic or aeroelastic transient type motions. A time-accurate alternating-direction implicit (ADI) finite-difference algorithm is used to solve the modified transonic small-disturbance equation

$$M^2(\phi_t + 2\phi_x)_t = [(1 - M^2)\phi_x + A\phi_x^2 + B\phi_y^2]_x + (\phi_y + C\phi_x\phi_y)_y + (\phi_z)_z \qquad (1)$$

where x, y, and z are the nondimensional physical coordinates in the streamwise, spanwise, and vertical directions, respectively. Several choices are available for the coefficients A, B, and C depending upon the assumptions used in deriving the TSD equation.[10] In this study, the coefficients are defined as

$$A = -\frac{1}{2}(\gamma + 1)M^2 \qquad (2a)$$

$$B = \frac{1}{2}(\gamma - 3)M^2 \qquad (2b)$$

$$C = -(\gamma - 1)M^2 \qquad (2c)$$

Boundary Conditions

Boundary conditions imposed upon the flow field are

Far upstream. $\phi = 0$ (3a)

Far downstream. $\phi_x + \phi_t = 0$ (3b)

Far above and below: $\phi_z = 0$ (3c)

Far spanwise: $\phi_y = 0$ (3d)

Symmetry plane. $\phi_y = 0$ (3e)

Trailing wake: $[\phi_z] = 0$ (3f)

$[\phi_x + \phi_t] = 0$ (3g)

where [ ] indicates the jump in the indicated quantity across the wake. The wing flow-

tangency boundary condition is

$$\phi_z^{\pm} = f_x^{+} + f_t^{\pm} \tag{4}$$

which is imposed at the mean plane of the wing.

Coordinate Transformation

The finite-difference grids in both the physical and computational domains are contained within rectangular regions and conform to the wing planform. Regions in the physical domain such as the swept and/or tapered wing are mapped into rectangular regions in the computational domain using the shearing transformation[13]

$$\xi = \xi(x,y), \quad \eta = y, \quad \zeta = z \tag{5}$$

where ξ, η, and ζ are the nondimensional computational coordinates in the streamwise, spanwise, and vertical directions, respectively. The TSD equation (Eq. (1)) may then be expressed in computational coordinates as

$$\begin{aligned} M^2 \frac{\partial}{\partial t}\left[\frac{1}{\xi_x}\phi_t + 2\phi_\xi\right] = \frac{\partial}{\partial \xi}\left[(1-M^2)\xi_x\phi_\xi + A\xi_x^2\phi_\xi^2\right. \\ + B(\xi_y\phi_\xi + \phi_\eta)^2 \\ \left. + \frac{\xi_y}{\xi_x}(\xi_y\phi_\xi + \phi_\eta) + C\xi_y\phi_\xi(\xi_y\phi_\xi + \phi_\eta)\right] \\ + \frac{\partial}{\partial \eta}\left[\frac{1}{\xi_x}(\xi_y\phi_\xi + \phi_\eta) + C\phi_\xi(\xi_y\phi_\xi + \phi_\eta)\right] \\ + \frac{\partial}{\partial \zeta}\left[\frac{1}{\xi_x}\phi_\zeta\right] \end{aligned} \tag{6}$$

Fuselage Modeling

In this study, the ADI solution procedure of the XTRAN3S code has been extended to allow the treatment of a fuselage. A discussion of fuselage modeling in small-disturbance codes and the development of the XTRAN3S wing-fuselage capability follow.

General Discussion. - For a fuselage at angle of attack α_F with unit normal vector $n = (n_x, n_y, n_z)$, the small-disturbance fuselage flow-tangency boundary condition may be written as

$$\phi_n = n_x + n_y\phi_y + n_z(\phi_z + \alpha_F) = 0 \tag{7}$$

where ϕ_n is the velocity normal to the surface. This boundary condition may be implemented in several different ways. For example, Eq. (7) may be imposed at boundary grid points identified to be in close proximity to the fuselage surface as done by Bailey and Ballhaus.[7] This method requires that a Cartesian grid be constructed such that points lie very close to the fuselage surface. This requirement is very restrictive, though, since it is difficult to construct such a grid in a Cartesian domain. Furthermore, the user is confronted with the same grid generation problem for each new configuration to be analyzed. An approach is desired that treats the fuselage with sufficient accuracy to obtain the correct global effect on the flow field without the use of special grids or complicated fuselage transformations.

Boppe[8] addressed the problem by imposing the fuselage boundary condition on a constant cross-section computational surface rather than on the true fuselage surface. The computational surface extends from upstream infinity to downstream infinity, the cross-section of which approximates the fuselage shape at the maximum fuselage diameter. This typically occurs in the wing-fuselage junction region. The technique is consistent with the small-disturbance approximation and since there is no requirement to locate grid points close to the fuselage surface, the method provides a "hands-off" representation for modeling wing-fuselage configurations. Obviously though, there are regions along the fuselage where the computational surface does not coincide with the true fuselage surface. This disparity is accounted for by correcting the fuselage boundary condition using slender body theory.

A further simplification to the implementation of Eq. (7) has been reported by Mason, et al.[14] in the user's manual for the Bailey/Ballhaus code. In Ref. 14, a fixed rectangular cross-section is used for the computational fuselage surface as shown in Fig. 1, rather than a shape determined at the maximum fuselage diameter. The advantage of this treatment is the simplification to the fuselage boundary condition (Eq. (7)) which results. Along the side boundary of the rectangular computational surface, Eq. (7) is approximated by

$$\phi_y = F_y \tag{8a}$$

and along the top and bottom boundaries, Eq. (7) is approximated by

$$\phi_z = F_z - \alpha_F \tag{8b}$$

where $F_y = -n_x/n_y$ and $F_z = -n_x/n_z$. These simplified fuselage boundary conditions are analogous to the wing flow-tangency boundary condition which is imposed on the mean plane of the wing rather than on the true wing surface. To account for spatial differences between true and computational fuselage surfaces, slender body theory corrections identical to those of Ref. 8 are applied. Separate corrections are imposed for fuselage thickness and fuselage incidence or angle of attack, which subsequently modify the terms which appear on the right-hand sides of Eqs. (8). Following Ref. 8, the correction applied to the fuselage thickness terms is derived by representing thickness by a source distribution with strength proportional to the rate of change of fuselage area. By requiring that the net source strength across the true and computational surfaces be equivalent at a given cross-section, the

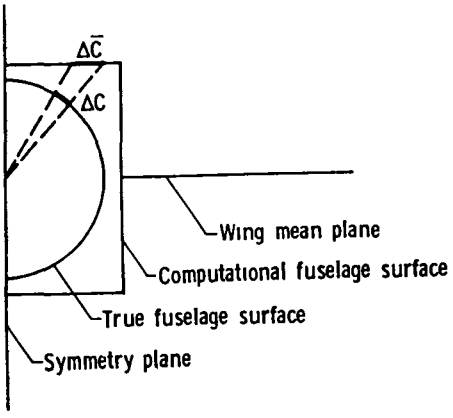

Fig. 1 Definition of arclengths on true and computational fuselage surfaces.

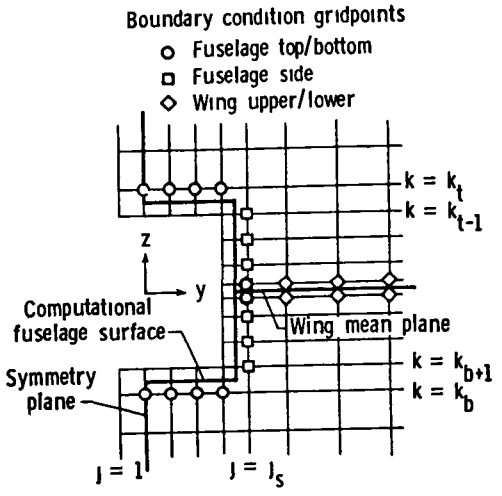

(a) sectional grid.

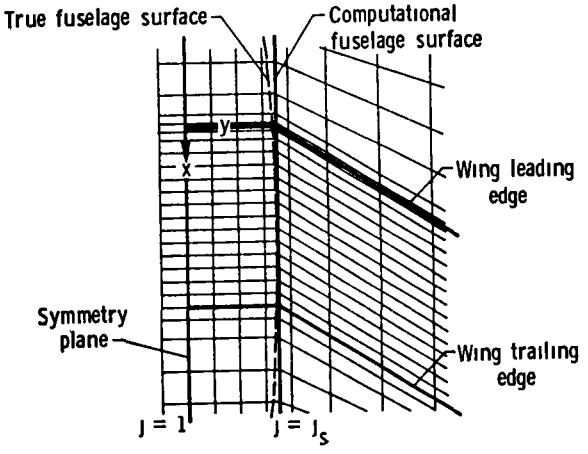

(b) planform grid.

Fig. 2 Treatment of grid to impose fuselage boundary conditions,

thickness terms F_y and F_z in Eqs. (8) are replaced by

$$\frac{\Delta C}{\Delta \bar{C}} F_y \tag{9a}$$

and

$$\frac{\Delta C}{\Delta \bar{C}} F_z \tag{9b}$$

where ΔC and $\Delta \bar{C}$ are arclengths of the true and computational fuselage surfaces, respectively, as graphically defined in Fig. 1. Similarly, the correction applied to the fuselage angle-of-attack term is derived by representing angle of attack by a doublet distribution with strength proportional to cross-sectional area. By equating doublet strengths, the angle-of-attack term in Eq. (8b) is replaced by

$$\frac{S(x)}{\bar{S}(x)} \alpha_F \tag{10}$$

where $S(x)$ and $\bar{S}(x)$ are the cross-sectional areas of the true and computational surfaces, respectively. Note that if these boundaries were to coincide, the original fuselage thickness and angle-of-attack terms are recovered since then $\Delta C = \Delta \bar{C}$ and $S = \bar{S}$. Including the slender body theory corrections, the fuselage boundary conditions become[14]

$$\phi_y = \xi_y \phi_\xi + \phi_\eta = \frac{\Delta C}{\Delta \bar{C}} F_y \tag{11a}$$

along the side surface and

$$\phi_z = \phi_\zeta = \frac{\Delta C}{\Delta \bar{C}} F_z - \frac{S}{\bar{S}} \alpha_F \tag{11b}$$

along the top and bottom surfaces.

Following Ref. 14, the boundary conditions (Eqs. (11)) have been incorporated in an implicit finite-difference fashion. This treatment of the fuselage imposes the boundary conditions directly within the ADI algorithm, which is in contrast with an approximate treatment using extrapolated differencing. The cross-plane (y-z) finite-difference grid is constructed so that the top, bottom, and side boundaries of the computational fuselage surface lie equidistantly between grid lines as shown in Fig. 2(a). The planform (x-y) finite-difference grid in the physical domain is constructed such that the grid is unswept in the region of the fuselage as shown in Fig. 2(b). Similar to the Bailey/Ballhaus code, the grid is unswept because of the implicit treatment of the fuselage side boundary condition. This requirement results since ϕ_y in Eq. (11a) becomes $\xi_y \phi_\xi + \phi_\eta$ in the computational domain, the two terms of which are treated separately in the ADI algorithm. In order to retain only the spanwise term ϕ_η, the grid is unswept so that $\xi_y = 0$ and the streamwise term vanishes.

In this study, the wing-fuselage grid typically contained 78 x 21 x 44 points in the x, y, and z directions, respectively, for a total of 72,072 grid points. This grid is considered to be coarse for such applications but reasonably adequate for demonstration purposes.

Top and Bottom Boundary Conditions. - The fuselage top and bottom boundary conditions are directly imposed within the differencing of the $\partial(\phi_\zeta)/\partial\zeta$ term in the TSD equation (Eq. (6)). This term is generally treated as

$$\frac{\partial}{\partial\zeta}(\phi_\zeta)_k = \frac{2}{\zeta_{k+1} - \zeta_{k-1}} \left(\phi_{\zeta_{k+1/2}} - \phi_{\zeta_{k-1/2}}\right) \quad (12)$$

where the derivatives on the right-hand side are written about half-node points. At grid points not involving the fuselage top and bottom boundary conditions, central-difference formulae are employed for these derivatives. At grid points just above the top boundary of the computational fuselage surface (ie., $k = k_t$ and $J < J_s$, as shown in Fig. 2(a)), the formula for the $\phi_{\zeta_{k-1/2}}$ derivative in Eq. (12) is replaced by the fuselage top boundary condition (Eq. (11b)). At grid points just below the bottom boundary of the computational fuselage surface (ie., $k = k_b$ and $J < J_s$, as shown in Fig. 2(a)), the formula for the $\phi_{\zeta_{k+1/2}}$ derivative in Eq. (12) is replaced by the fuselage bottom boundary condition (Eq. (11b)).

Side Boundary Condition. - The fuselage side boundary condition is directly imposed within the differencing of the $\partial(\phi_\eta)/\partial\eta$ term as well as all of the single-derivative-with-respect-to-η terms in the TSD equation (Eq. (6)). The second-derivative term is generally treated as

$$\frac{\partial}{\partial\eta}(\phi_\eta)_J = \frac{2}{\eta_{J+1} - \eta_{J-1}} \left(\phi_{\eta_{J+1/2}} - \phi_{\eta_{J-1/2}}\right) \quad (13)$$

where the derivatives on the right-hand side are written about half-node points. At grid points not involving the fuselage side boundary condition, central-difference formulae are employed for these derivatives. At grid points adjacent to the side boundary of the computational fuselage surface (ie., $J = J_s$ and $k_b < k < k_t$, as shown in Fig. 2(a)), the formula for the $\phi_{\eta_{J-1/2}}$ derivative in Eq. (13) is replaced by the fuselage side boundary condition (Eq. (11a)). The single-derivative-with-respect-to-η terms are generally treated using central-difference operators of the form

$$\frac{\partial}{\partial\eta}(\phi)_j = \frac{1}{\eta_{J+1} - \eta_{J-1}} \left(\phi_{J+1} - \phi_{J-1}\right) \quad (14)$$

where the terms on the right-hand side are written at full-node points. These operators must be modified at grid points adjacent to the side boundary because they contain potentials ϕ_{J-1}, which lie inside the computational fuselage surface. Equation (14) may be rewritten, though, as a weighted average of η-derivatives at the half-node points as

$$\frac{\partial}{\partial\eta}(\phi)_J = \left(\frac{\eta_{J+1} - \eta_J}{\eta_{J+1} - \eta_{J-1}}\right)\phi_{\eta_{J+1/2}} + \left(\frac{\eta_J - \eta_{J-1}}{\eta_{J+1} - \eta_{J-1}}\right)\phi_{\eta_{J-1/2}} \quad (15)$$

Therefore, at grid points adjacent to the side boundary of the computational fuselage surface, the $\phi_{\eta_{J-1/2}}$ derivatives are replaced by Eq. (11a).

The XTRAN3S code now is capable of computing unsteady transonic flow fields about wing-fuselage configurations. The capability can treat wings that are high, low, or mid-mounted, although all of the results presented are for mid-mounted configurations. The fuselage modeling is also general enough to treat fairly arbitrary fuselage cross-sections, although the present results were obtained for fuselages with circular cross-sections. The formulation can easily treat more complex geometries, since the construction of the finite-difference grid and the treatment of the fuselage boundary conditions remain the same.

Pressure Coefficient Calculations

The pressure coefficients on the upper and lower surfaces of the wing are calculated using

$$C_p = -2(\phi_x + \phi_t) - (1 - M^2)\phi_x^2 \quad (16)$$

The second-order term in the streamwise direction has been retained in this study to improve accuracy and has been added to the first-order formula already available within XTRAN3S.

The pressure coefficients on the surface of the fuselage are computed using

$$C_p = -2(\phi_x + \phi_t) - (1 - M^2)\phi_x^2 - \phi_y^2 - \phi_z^2 + M^2\phi_t^2 + 2M^2\phi_x\phi_t \quad (17)$$

which includes all of the second-order terms. Since grid lines are not placed on the boundaries of the computational fuselage surface, the velocity potential is not directly calculated there. The potential along the surface is determined by using the boundary conditions and assuming that the velocity potential varies linearly between the surface and the adjacent grid line. This leads to simple formulae for the determination of the surface potential. On the top boundary of the computational fuselage surface, for example, the velocity potential is calculated using

$$\phi_{top} = \phi_{k_t} - \frac{1}{2}\left(\zeta_{k_t} - \zeta_{k_{t-1}}\right)\left(\frac{\Delta C}{\Delta\bar{C}} F_z - \frac{S}{\bar{S}} \alpha_F\right) \quad (18)$$

Also, the derivatives in Eq. (17) must be evaluated, not on the computational fuselage surface where the velocity potential can be calculated, but on the true fuselage surface. Since the true and computational fuselage surfaces do not generally coincide, the derivatives on the true surface are, therefore, determined using Taylor series expansions of the derivatives, truncated to first-order. For the true surface of the fuselage, for example, the ϕ_x term in Eq. (17) is calculated using

$$\phi_{x_{true}} = \phi_{x_{comp}} - \Delta y\, \phi_{xy_{comp}} - \Delta z\, \phi_{xz_{comp}} \qquad (19)$$

where Δy and Δz are distances between the true and computational surfaces in the y and z directions, respectively.

Structural Modes

Unsteady transonic calculations were performed for first bending and first torsion modal oscillations of the wing. For demonstration purposes, simple polynomial equations were assumed to describe the modes. The wing was assumed to be rigidly attached to the fuselage. The equation defining the first bending mode shape was derived by further assuming that the node line is perpendicular to the wing midchord line at the root. The resulting expression for the first bending mode shape is given by

$$f_h = (y-y_r)\left[(x-\tfrac{1}{2})\sin\Lambda_{c/2} + (y-y_r)\cos\Lambda_{c/2}\right] \quad \text{for } y \geq y_r \qquad (20)$$

where y_r is the spanwise coordinate of the wing root and $\Lambda_{c/2}$ is the sweep angle of the wing midchord line. The equation defining the first torsion mode shape, derived by assuming that the node line coincides with the wing midchord line, is given by

$$f_\alpha = (y-y_r)\left[(x-\tfrac{1}{2})\cos\Lambda_{c/2} - (y-y_r)\sin\Lambda_{c/2}\right] \quad \text{for } y \geq y_r \qquad (21)$$

Equations (20) and (21) were normalized to give unit deflection and unit twist, respectively, at the tip. The tip amplitude of the torsion mode was selected as 1° and the amplitude of the bending mode was calculated to be an equivalent effective angle of attack using $\dot{h}_{tip}/U = 1°$.

Results and Discussion

Configurations

Results are presented for the three wing-fuselage configurations shown in Fig. 3. These configurations were selected to assess the fuselage treatment and verify the code modifications to XTRAN3S by making comparisons with the experimental steady pressure data of Refs. 15-17. The first configuration (Fig. 3(a)) is the Wall Interference Model[15] tested at the Arnold Engineering Development Center (AEDC) (hereafter referred to as the AEDC wing-fuselage) which consists of a rectangular-planform wing that is centrally mounted on a circular cross-section sting-body. As listed in Fig. 3(a), the wing has a NACA 63A006 airfoil section, a leading edge sweep angle of 0°, a full-span aspect ratio of 3.56, and a taper ratio of 1.0. The axisymmetric fuselage has a fineness ratio (length/maximum diameter) of 8.42. A more detailed description of the AEDC wing-fuselage is reported in Ref. 15 along with the experimental data. The second configuration (Fig. 3(b)) is that of a transonic wing-fuselage model tested in the NACA Langley 8-Foot High Speed Tunnel.[16] The model, hereafter referred to as the NACA wing-fuselage, consists of a swept tapered wing that is centrally mounted on an axisymmetric fuselage. As listed in Fig. 3(b), the wing has a NACA 65A006 airfoil section, a leading edge sweep angle of 46.76°, an aspect ratio of 4.0, and a taper ratio of 0.6. The fuselage has circular cross-sections and a basic fineness ratio of 12.0. The NACA wing-fuselage geometry is further described in Ref. 16. The third configuration, shown in

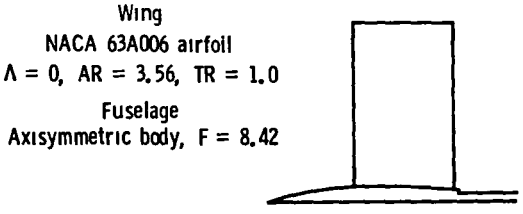

(a) AEDC.

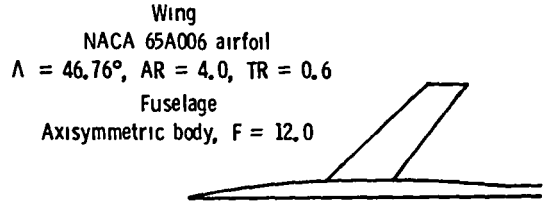

(b) NACA.

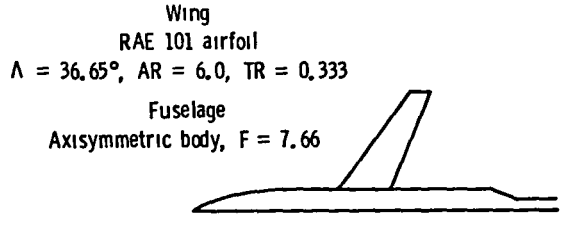

(c) RAE.

Fig. 3 Wing-fuselage configurations;

Fig. 3(c), is a transport-type wing-fuselage model that was tested in the Royal Aircraft Establishment (RAE) 8 ft. x 6 ft. Transonic Wind Tunnel. This model (hereafter referred to as the RAE wing-fuselage) is a standard configuration of the AGARD Fluid Dynamics Panel and consists of the RAE wing "A" in combination with an axisymmetric body.[17] As listed in Fig. 3(c), the wing of the RAE wing-fuselage has an RAE 101 airfoil section, a leading edge sweep angle of 36.65°, an aspect ratio of 6.0, and a taper ratio of one-third. The fuselage has a fineness ratio of 7.66 and a constant diameter from 0.35 L to 1.0 L. The fuselage is mounted to the sting using a short tapered section as shown in Fig. 3(c). Although the stings for the three wing-fuselage configurations are modeled using XTRAN3S, the short tapered section connecting the fuselage of the RAE model to the sting was not. This section was neglected to minimize the cost of the calculations since fewer gridpoints are required. Furthermore, no experimental data was measured aft of 0.83 L on the fuselage.

Parallel calculations were also performed for the NACA and RAE configurations without the fuselages, to assess the effects of fuselage aerodynamic interference by making comparisons with the wing-fuselage results. These wing-alone calculations were performed for the exposed wing planform, with a plane of symmetry assumed at the wing root.

AEDC Wing-Fuselage

Steady transonic calculations were performed for the AEDC wing-fuselage for comparison with the experimental data of Ref. 15. The experimental steady pressure data was measured at the midsemispan of the wing and the fuselage symmetry plane only. Two cases were considered to validate the XTRAN3S wing-fuselage capability. The first case, Case 1 of Table 1, was chosen to assess the XTRAN3S fuselage thickness modeling by selecting zero mean angle of attack for the wing and fuselage. This produces a symmetric flow above and below the wing-fuselage such that the upper and lower surface pressures are identical. The second case, Case 2 of Table 1, was selected to assess the fuselage angle-of-attack modeling. For both cases, the time step was $\Delta t = 0.05$, and 800 steps were required for the solution to converge.

Table 1 Wing-fuselage configurations and computational conditions for transonic aerodynamic analyses.

Wing-fuselage	Case	M	α_W, α_F
AEDC	1	0.9	0°
	2	0.8	2.663°
NACA	3	0.93	2°
RAE	4	0.9, 0.91	0°
	5	0.9, 0.91	1°

In Case 1, the freestream Mach number was 0.9 and $\alpha_W = \alpha_F = 0$. Comparisons between XTRAN3S and experimental steady pressure distributions are shown in Figs. 4(a) and 4(b) for the wing and fuselage, respectively. For the wing (Fig. 4(a)), the XTRAN3S pressures compare well with the experimental data. There is a relatively strong shock wave on the upper and lower surfaces near 65-70% chord. The XTRAN3S comparison with experiment is typical for a conservative inviscid TSD code in that the calculated shocks are located slightly aft of the experimental location and the post-shock pressures are slightly overpredicted. For the fuselage (Fig. 4(b)), the symmetry plane pressure distribution resembles that of the wing in the region of the wing location, and there is a relatively strong shock wave on the fuselage upper and lower surfaces near 0.66 L. The XTRAN3S fuselage pressure distribution is in good agreement with the experimental data. This

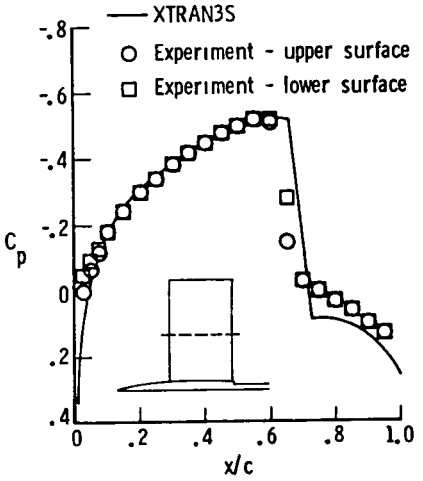

(a) wing midsemispan.

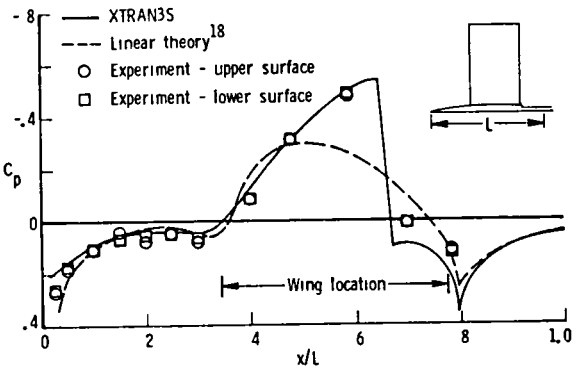

(b) fuselage symmetry plane.

Fig. 4 Comparison between XTRAN3S and experimental steady pressure distributions on the AEDC wing-fuselage at M = 0.9 and $\alpha_W = \alpha_F = 0$,

agreement is as good as that for the wing which thus verifies the fuselage thickness modeling. Also, linear theory results from Ref. 18, computed using the Woodward[3] panel code, are presented in Fig. 4(b) for further comparison. The linear theory results compare well with the experimental pressures except in the wing location region where transonic effects are important.

In Case 2, the freestream Mach number was 0.8 and the experimental data was obtained at 2° angle of attack. The calculations, though, were performed at a corrected angle of attack of 2.663° to include the static deformation of the sting under load.[18] The wing midsemispan and fuselage symmetry plane steady pressure distributions are shown in Figs. 5(a) and 5(b), respectively. For the wing (Fig. 5(a)), the XTRAN3S pressures are in good general agreement with the experimental data except for a slight

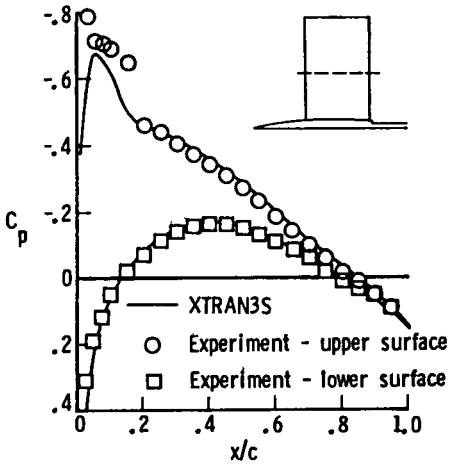

(a) wing midsemispan.

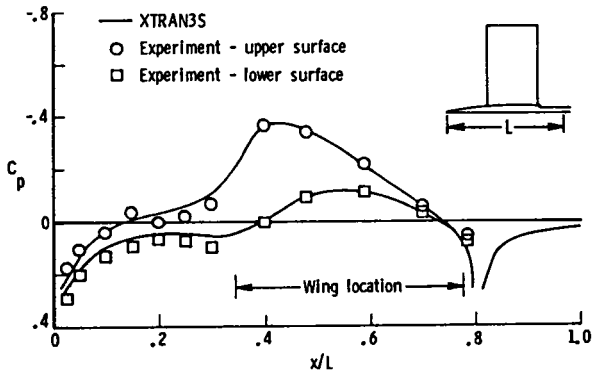

(b) fuselage symmetry plane.

Fig. 5 Comparison between XTRAN3S and experimental steady pressure distributions on the AEDC wing-fuselage at M = 0.8 and $\alpha_W = \alpha_F = 2.663°$;

underprediction of the leading edge suction peak on the upper surface. For the fuselage (Fig. 5(b)), the XTRAN3S calculations compare very well with the experimental steady pressure data along both the upper and lower fuselage surfaces. The good agreement between XTRAN3S and experimental symmetry plane pressures thus verifies the fuselage angle-of-attack modeling.

NACA Wing-Fuselage

Steady transonic calculations were performed for the NACA wing-fuselage for comparison with the experimental data of Ref. 16. This configuration is a more challenging case for assessment of the wing-fuselage capability due to the high sweep of the wing. Calculations were performed at M = 0.93 and $\alpha_W = \alpha_F = 2°$, which is referred to as Case 3 as listed in Table 1. The time step was $\Delta t = 0.01$, and 2400 steps were required to obtain a converged solution. Comparisons between XTRAN3S and experimental steady pressure distributions for five span stations along the wing are given in Fig. 6. Calculations for the wing-alone configuration are also plotted for further comparison. For Case 3, the flow is supercritical over a large portion of the upper surface of the wing and the experimental data indicates that there is a very mild shock wave on the upper surface between approximately $\bar{\eta}$ = 0.40 and $\bar{\eta}$ = 0.60. As shown in Fig. 6, the XTRAN3S steady pressures compare reasonably well with the experimental data. The wing-fuselage calculations are in slightly better agreement with the experiment than the wing-alone calculations. Differences between the wing-alone and wing-fuselage calculated steady pressure distributions represent the aerodynamic interference of the fuselage on the wing. For Case 3, the effect of the fuselage increases (negatively) the pressure coefficients on both the upper and lower surfaces of the wing. The effect is largest on the inboard portion of the wing and decreases slightly outboard toward the tip. The fuselage interference effect is still noticeable at $\bar{\eta}$ = 0.95, though, near the leading edge of the wing upper surface. Shown in Fig. 7 are the fuselage symmetry plane steady pressure distributions for Case 3. The fuselage pressure values are generally small for this case except in the wing location region where a pressure expansion on both upper and lower surfaces is produced by the disturbance of the wing. In general, the XTRAN3S fuselage pressure distributions are in fair agreement with the experimental data. Differences between the calculated and experimental pressures are attributed in part to the coarseness of the grid.

RAE Wing-Fuselage

Transonic calculations were performed for the RAE wing-fuselage to further assess the wing-fuselage capability. Two cases were selected for comparison with the experimental steady pressure data of Ref. 17. The two cases (4 and 5 of Table 1) correspond to the wing-fuselage at 0° and 1° mean angles of attack. For both cases, the time step was Δt = 0.025 and 1600 steps were used to obtain a converged solution. The experimental data was measured at a freestream Mach number of 0.9 and

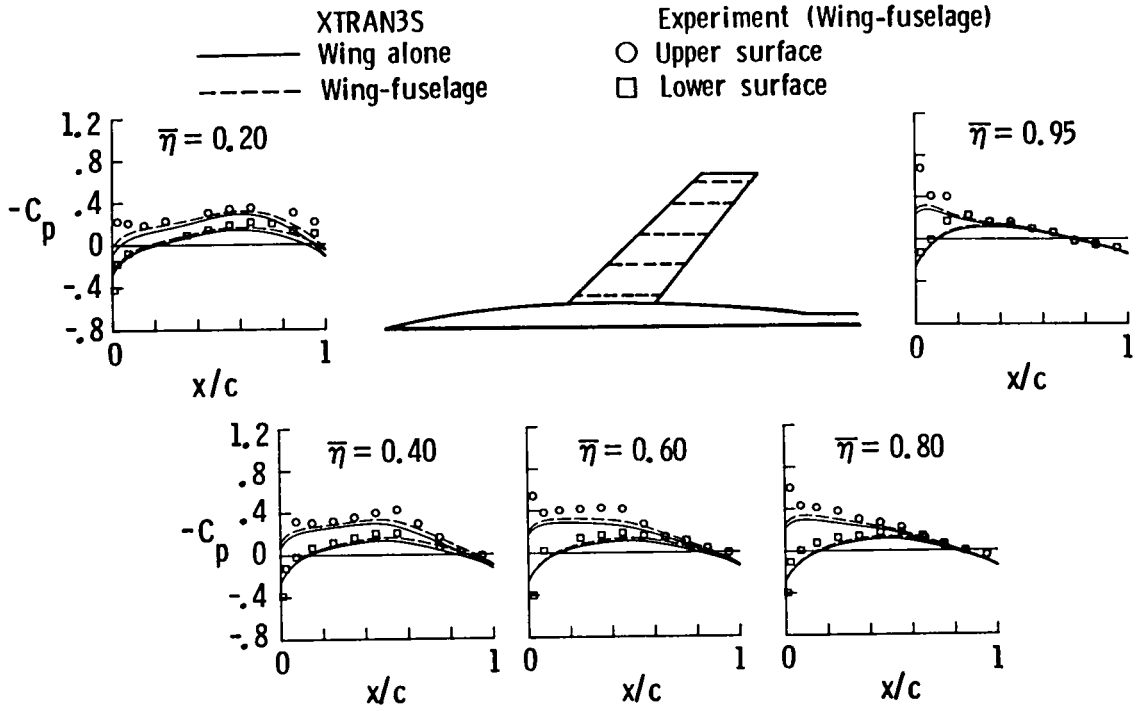

Fig. 6 Comparison between XTRAN3S and experimental wing steady pressure distributions on the NACA wing-fuselage at M = 0.93 and $\alpha_W = \alpha_F = 2°$.

the calculations were performed at both M = 0.9 and M = 0.91. Calculations were made at the latter Mach number since it was shown in Ref. 14 that results computed using the Bailey/Ballhaus code for the RAE wing-fuselage at M = 0.91 were in better agreement with the experimental data than results computed at M = 0.9.

Steady pressure distributions for six span stations along the wing of the RAE wing-fuselage are plotted in Fig. 8 for Case 4. The pressure distributions indicate that the flow is supercritical over a small portion of the upper and lower surfaces of the wing. The XTRAN3S

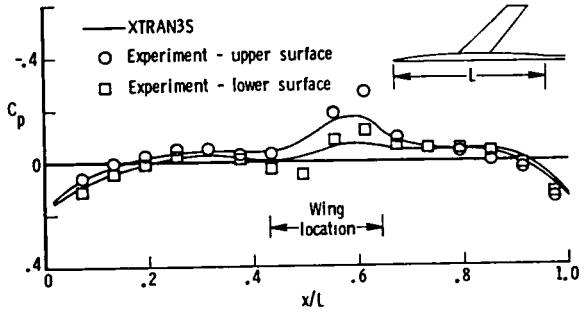

Fig. 7 Comparison between XTRAN3S and experimental fuselage symmetry plane steady pressure distributions on the NACA wing-fuselage at M = 0.93 and $\alpha_W = \alpha_F = 2°$.

pressures are in good agreement with the experimental data, with the largest differences occurring in the outboard region of the wing near the tip ($\bar{\eta}$ = 0.925). Although the calculations at M = 0.9 compare better with the experimental data inboard on the wing (at $\bar{\eta}$ = 0.25, for example), the calculations at M = 0.91 are generally in better overall agreement with the experiment. Figure 9 shows the fuselage symmetry plane steady pressure distributions at M = 0.9. There is a large pressure expansion from 0.11 to 0.40 L due to the sloped nose of the fuselage. The expansion in the wing location region results from the disturbance created by the wing. In general, the XTRAN3S fuselage pressures agree well with the experimental data.

Steady pressure distributions at $\bar{\eta}$ = 0.25 of the wing are presented for Case 4 in Fig. 10. Calculated results for M = 0.9 are plotted for both the wing-alone and wing-fuselage configurations for comparison with the experimental data. As shown in Fig. 10, the XTRAN3S wing-fuselage pressures are in better agreement with the experiment than the wing-alone pressures. For the RAE wing-fuselage, the aerodynamic interference of the fuselage decreases the magnitude of the wing steady pressure coefficients in the inboard region of the wing which is opposite to that found for the NACA wing-fuselage (Fig. 6). This effect decreases rapidly along the span and is negligible at the tip (not shown).

Steady pressure distributions for the RAE wing-fuselage are shown in Fig. 11 for Case 5.

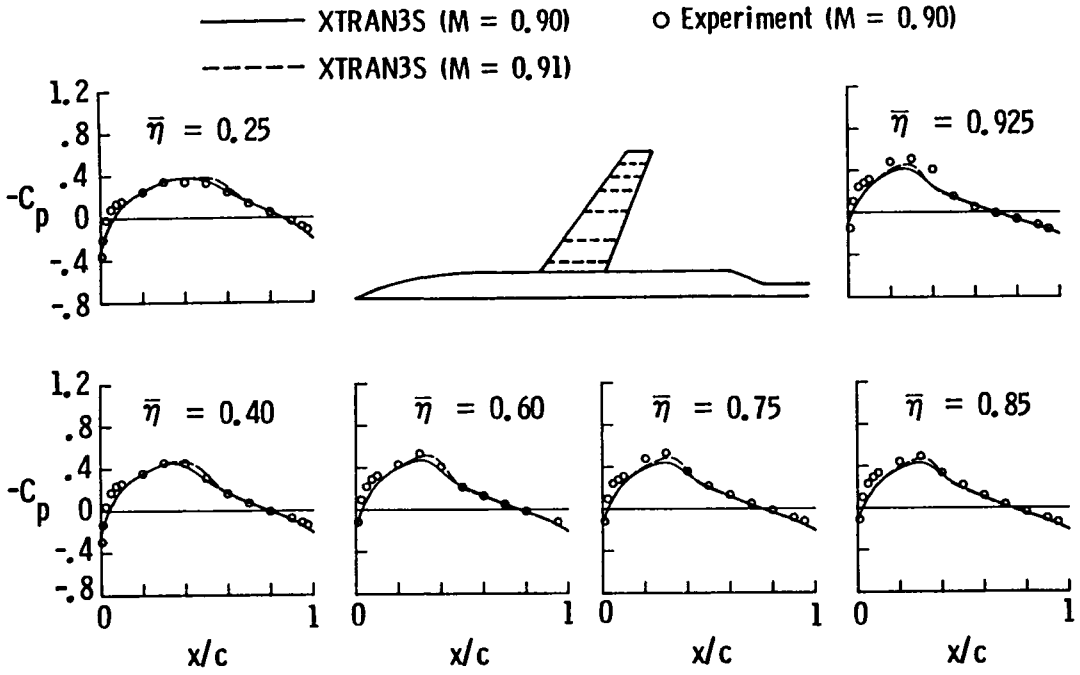

Fig. 8 Comparison between XTRAN3S and experimental wing steady pressure distributions on the RAE wing-fuselage at M = 0.90, 0.91, and $\alpha_W = \alpha_F = 0$.

There is a shock wave on the upper surface of the wing that is relatively mild in the inboard region and is of moderate strength outboard toward the wing tip. In general, the XTRAN3S steady pressures are in good agreement with the experimental data. The calculations at M = 0.9 compare better with the experiment in the inboard region of the wing (at $\bar{\eta}$ = 0.25, for example), but the calculated results at M = 0.91 are generally what is expected from a conservative inviscid TSD code in comparison with the experiment. For example, the shock wave on the wing upper surface calculated at M = 0.91 is located slightly aft of the experimental location and the post-shock pressures are overpredicted. For cases such as this, the inclusion of the nonisentropic effects and viscous effects is required to improve the correlation between calculation and experiment. Figure 12 shows the fuselage symmetry plane steady pressure distributions at M = 0.9 and $\alpha_W = \alpha_F = 1°$ (Case 5). These pressure distributions are very similar to those at zero angle of attack shown in Fig. 9. In this case, the fuselage carries a small amount of lift in the wing location region. In general, the XTRAN3S fuselage pressures are in reasonably good agreement with the experimental data.

Steady pressure distributions at $\bar{\eta}$ = 0.25 of the wing are presented in Fig. 13 for Case 5. The calculated pressure distributions for M = 0.9 are plotted for the wing-alone and

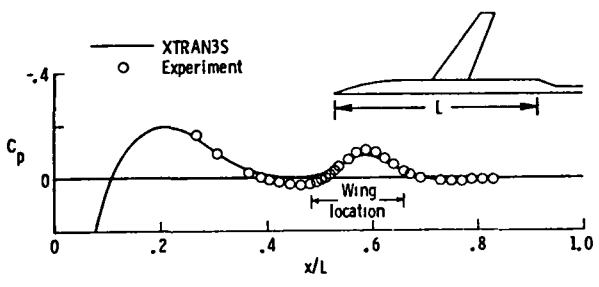

Fig. 9 Comparison between XTRAN3S and experimental fuselage symmetry plane steady pressure distributions on the RAE wing-fuselage at M = 0.9 and $\alpha_W = \alpha_F = 0$.

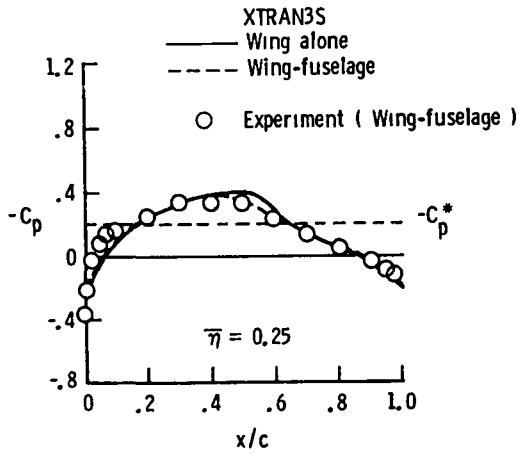

Fig. 10 Wing steady pressure distributions for the RAE wing-fuselage at M = 0.9, $\alpha_W = \alpha_F = 0$, and $\bar{\eta}$ = 0.25.

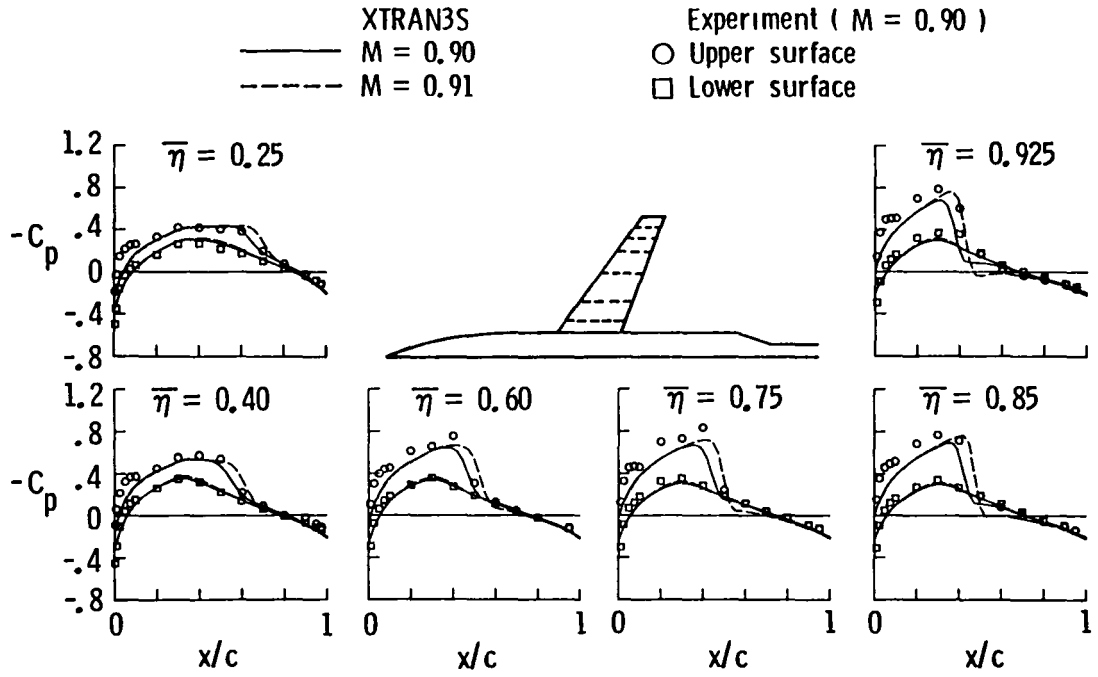

Fig. 11 Comparison between XTRAN3S and experimental wing steady pressure distributions on the RAE wing-fuselage at M = 0.90, 0.91, and $\alpha_W = \alpha_F = 1°$.

wing-fuselage configurations for comparison with the experimental data. As shown in Fig. 13, the fuselage interference weakens the mild shock wave on the wing upper surface bringing the XTRAN3S steady pressures into very good agreement with the experiment. In fact, the calculated pressure distributions for the wing-fuselage agree better with the experiment for both upper and lower surfaces in comparison with the wing-alone results.

Unsteady transonic calculations were performed for the RAE wing-fuselage to demonstrate application of the new capability to aeroelastic problems. Experimental data for this model are not available for comparison purposes. The freestream Mach number was selected as M = 0.91 and $\alpha_W = \alpha_F = 1°$ (Case 5). The wing was first forced to oscillate harmonically in first bending and then in first torsion, at a reduced frequency of k = 0.25. The time step was $\Delta t = 0.02513$ which results in 500 steps per cycle of motion. Three cycles of motion were computed to obtain a periodic solution. The wing-fuselage calculations are compared with wing-alone results to determine the effects of fuselage aerodynamic interference on unsteady wing loading.

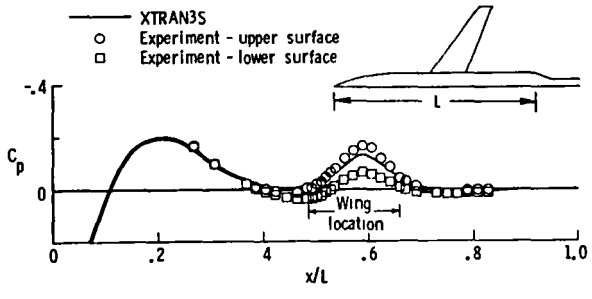

Fig. 12 Comparison between XTRAN3S and experimental fuselage symmetry plane steady pressure distributions on the RAE wing-fuselage at M = 0.9 and $\alpha_W = \alpha_F = 1°$.

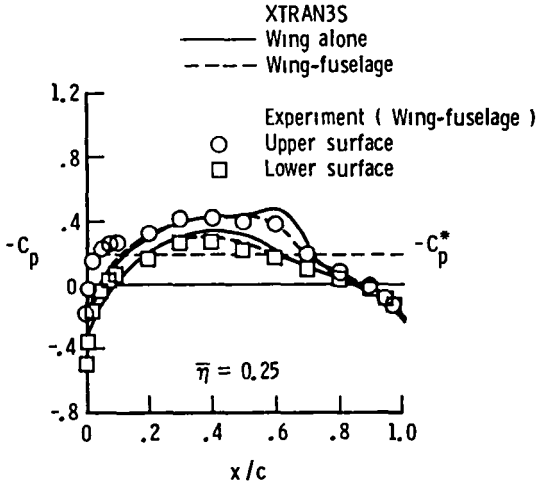

Fig. 13 Wing steady pressure distributions for the RAE wing-fuselage at M = 0.9, $\alpha_W = \alpha_F = 1°$, and $\overline{\eta} = 0.25$.

Unsteady sectional lift and moment coefficients are shown in Figs. 14(a) and 14(b), respectively, for the wing oscillating in its first bending mode. These coefficients are plotted as real (in-phase) and imaginary (out-of-phase) components of the spanwise wing loading. The unsteady coefficients are largest in the outboard region of the wing since the wing motion is largest at the tip. The effect of fuselage aerodynamic interference is generally largest inboard towards the wing-fuselage junction, as expected. As shown in Fig. 14(a), for example, the fuselage interference decreased the magnitudes of the real and imaginary lift coefficients by 19% and 37%, respectively, near the wing-fuselage junction. In the middle region of the wing, the real part of c_ℓ is decreased and the imaginary part is increased when the fuselage is included in the calculation. These changes in the real and imaginary parts occur such that the magnitude of c_ℓ is slightly decreased and the phase of c_ℓ is increased due to fuselage interference. The interference effect attenuates along the span and is negligible outboard toward the wing tip. The effect of the fuselage on the unsteady sectional moment coefficients (Fig. 14(b)) is similar to that on the lift coefficients. The magnitudes of the real and imaginary components of c_m are decreased near the wing-fuselage junction for the wing-fuselage configuration and the effect

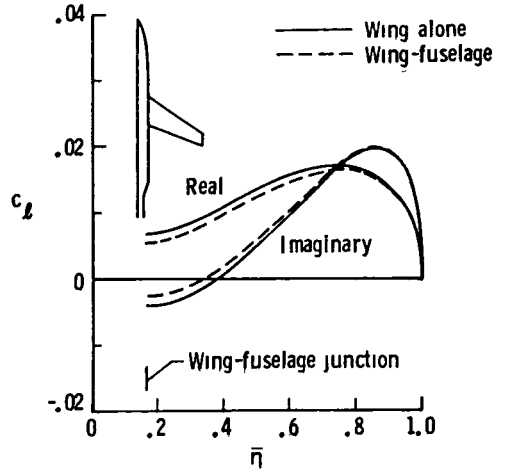

(a) sectional lift coefficients.

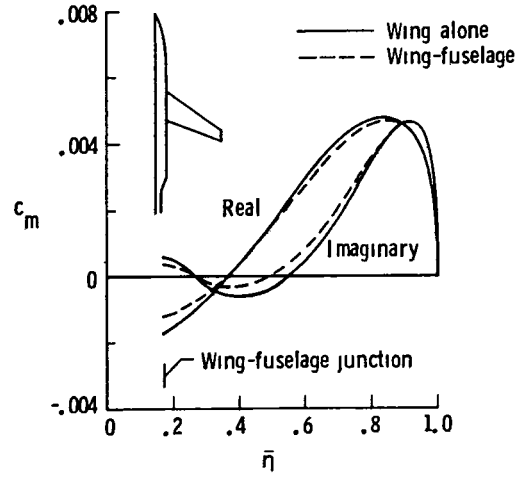

(b) sectional moment coefficients.

Fig. 14 Unsteady sectional coefficients due to wing first bending for the RAE wing-fuselage at M = 0.91, $\alpha_W = \alpha_F = 1°$ and k = 0.25;

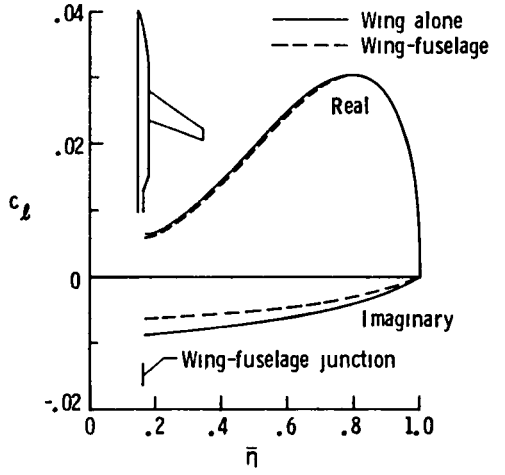

(a) sectional lift coefficients.

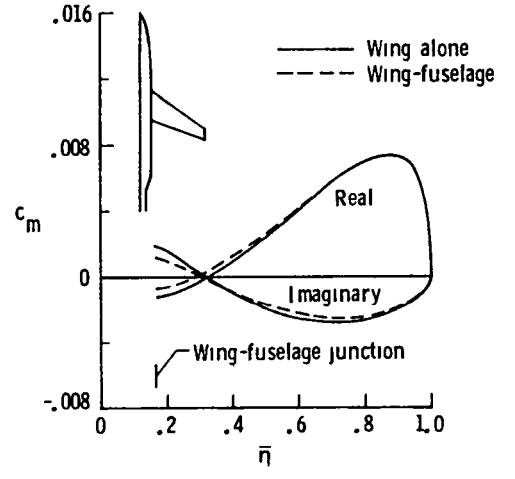

(b) sectional moment coefficients.

Fig. 15 Unsteady sectional coefficients due to wing first torsion for the RAE wing-fuselage at M = 0.91, $\alpha_W = \alpha_F = 1°$ and k = 0.25;

generally decreases spanwise, vanishing near the tip.

Unsteady sectional lift and moment coefficients are shown in Figs. 15(a) and 15(b), respectively, for the wing oscillating in its first torsion mode. These coefficients are similar in character to the coefficients of Fig. 14 in that the largest magnitudes generally occur in the outboard region since the motion of the wing is largest at the tip. The effects of fuselage aerodynamic interference are greatest in the inboard region near the wing-fuselage junction. As shown in Fig. 15(a), for example, the fuselage interference slightly lowers the real part of c_ℓ and significantly decreases the magnitude of the imaginary part. The total magnitude of the sectional lift coefficients is thereby reduced and the phase increased when the fuselage is included in the calculation. This result is attributed physically to the weakening of the steady shock on the wing by the presence of the fuselage as shown in the steady pressure distributions of Fig. 13. For the moment coefficients (Fig. 15(b)), the fuselage interference decreased the magnitudes of the real and imaginary components near the wing-fuselage junction. Outboard on the wing, the effect of the fuselage is small.

Generalized aerodynamic forces were then calculated by integrating the unsteady lifting pressures weighted by the mode shapes, over the wing planform. These forces A_{ij} are typically used in flutter analyses and are defined as the forces resulting from the pressure induced by mode j acting through the displacements of mode i. In this study bending and torsion are defined as modes 1 and 2, respectively. The generalized aerodynamic forces are listed in Table 2 for both the wing-alone and wing-fuselage cases. Results are tabulated in both real, imaginary and magnitude, phase forms to allow for a fair and complete assessment of fuselage aerodynamic interference. Comparisons between the forces indicate relatively small changes in the real components and generally much larger changes in the imaginary components when the fuselage is included in the calculation. For example, the imaginary part of A_{12} is decreased 29.7% and the imaginary part of A_{21} is increased 27.3%. In general, though, the changes in the generalized aerodynamic forces occur such that the total magnitude is increased 2 to 5%, and the phase is increased 2 to 3°.

Concluding Remarks

A time-accurate transonic wing-fuselage capability has been developed for unsteady aerodynamic and aeroelastic applications. The new capability was developed by extending the XTRAN3S unsteady transonic small-disturbance code to allow the treatment of a fuselage. The code is now capable of computing unsteady transonic flow fields about wing-fuselage configurations. The capability permits the assessment of fuselage aerodynamic interference effects on transonic unsteady airloads and flutter characteristics of wings.

Steady transonic calculations were presented for three wing-fuselage geometries with leading edge sweep angles ranging from 0° to 46.76° and comparisons were made with experimental pressure data for code validation purposes. The XTRAN3S wing and fuselage pressure distributions were in good agreement with the experimental data. These favorable comparisons thus verify the fuselage treatment and code modifications to XTRAN3S, and also demonstrate the accuracy of the code for wing-fuselage applications. Furthermore, comparisons of steady pressure distributions calculated using XTRAN3S both with and without the fuselage revealed the effects of fuselage steady aerodynamic interference on the wing. In general the interference of the fuselage on the wing pressures was largest inboard near the wing-fuselage junction and attenuated outboard toward the wing tip, as expected.

Unsteady transonic calculations were presented for a transport-type wing-fuselage configuration. The calculations were performed for simple first bending and first torsion structural modes that were assumed for the wing. Comparisons of unsteady sectional lift and moment coefficients for the wing-alone and wing-fuselage cases revealed effects of fuselage aerodynamic interference on the unsteady wing loading. In general, the interference of the fuselage decreased the magnitude of the lift and moment coefficients near the wing-fuselage junction. The effect of the fuselage on the unsteady wing loading decreased outboard towards the wing tip, similar to the attenuation of the effect on the steady pressures. Tabulated generalized aerodynamic forces, typically used in flutter analyses, indicated small changes in the real component and as much as a 30% change

Table 2 Generalized aerodynamic forces for RAE wing-fuselage at M = 0.91, $\alpha_W = \alpha_F = 1°$, and k = 0.25 (mode 1 bending, mode 2 torsion).

A_{ij}		Wing-alone				Wing-fuselage						
i	j	Real	Imag.	Mag.	Phase	Real	% Increase	Imag	% Increase	Mag.	% Increase	Phase	degree Increase
1	1	.230	.254	.343	47.8°	.227	-1.3	.270	6.3	.353	2.9	49.9°	2.1
1	2	.841	-.101	847	-6.9°	858	2.0	-.071	29.7	.861	2.4	-4.7°	2.2
2	1	.037	.011	.039	17.0°	.038	2.7	.014	27.3	.041	5.1	19.9°	2.9
2	2	.095	- 076	.121	-38.6°	.101	6.3	-.073	-3.9	.124	2.5	-35.7°	2.9

in the imaginary component when the fuselage was included in the calculation. These changes resulted in a 2 to 5% increase in total magnitude and a several degree increase in phase.

The work was conducted as part of a larger effort directed toward developing the capability to treat a complete flight vehicle. Future work will be aimed at applications to more complex wing-fuselage geometries and developing a wing-fuselage-tail capability.

References

[1]Giesing, J. P.; Kalman, T. P., and Rodden, W. P.: "Subsonic Steady and Oscillatory Aerodynamics for Multiple Interfering Wings and Bodies." Journal of Aircraft, Vol. 9, No. 10, October 1972, 693-702.

[2]Woodward, F. A.· "Analysis and Design of Wing-Body Combinations at Subsonic and Supersonic Speeds." Journal of Aircraft, Vol. 5, No. 6, November - December, 1968, pp. 528-534.

[3]Woodward, F. A.· "An Improved Method for the Aerodynamic Analysis of Wing-Body-Tail Configurations in Subsonic and Supersonic Flows." NASA CR-2228, May 1973.

[4]Dusto, A. R.; and Epton, M. A.· "An Advanced Panel Method for Analysis of Arbitrary Configurations in Unsteady Subsonic Flow." NASA CR-152323, February 1980.

[5]Bailey, F. R., and Ballhaus, W. F.· "Relaxation Methods for Transonic Flow About Wing-Cylinder Combinations and Lifting Swept Wings." Lecture Notes in Physics, Vol. 19, Springer-Verlag, 1972, pp. 2-9.

[6]Klunker, E. B.; and Newman, P. A. "Computation of Transonic Flow About Lifting Wing-Cylinder Combinations." Journal of Aircraft, Vol. 11, No. 4, April 1974, pp. 254-256.

[7]Bailey, F. R., and Ballhaus, W. F. "Comparisons of Computed and Experimental Pressures for Transonic Flows About Isolated Wings and Wing-Fuselage Configurations." NASA SP-347, March 1975, pp. 1213-1231.

[8]Boppe, C. W.: "Computational Transonic Flow About Realistic Aircraft Configurations." AIAA Paper No. 78-104, Presented at the AIAA 16th Aerospace Sciences Meeting, Huntsville, Alabama, January 16-18, 1978.

[9]Boppe, C. W., and Stern, M. A. "Simulated Transonic Flows for Aircraft with Nacelles, Pylons, and Winglets." AIAA Paper No. 80-0130, Presented at the AIAA 18th Aerospace Sciences Meeting, Pasadena, California, January 14-16, 1980.

[10]Borland, C. J.; and Rizzetta, D. P.· "Nonlinear Transonic Flutter Analysis." AIAA Journal, Vol. 20, No. 11, November 1982, pp. 1606-1615.

[11]Batina, J. T.· "Unsteady Transonic Flow Calculations for Interfering Lifting Surface Configurations." AIAA Paper No. 85-1711, Presented at the AIAA 18th Fluid Dynamics, Plasmadynamics, and Lasers Conference, Cincinnati, Ohio, July 16-18, 1985. Also available as NASA TM 86432, May 1985.

[12]Guruswamy, G. P., Goorjian, P. M.; and Tu, E. L. "Unsteady Transonics of a Wing With Tip Store," AIAA Paper No. 86-0010, Presented at the AIAA 24th Aerospace Sciences Meeting, Reno, Nevada, January 6-9, 1986.

[13]Borland, C. J. "Further Development of XTRAN3S Computer Program." NASA CR 172335, May 1984.

[14]Mason, W. H.; Mackenzie, C.; Stern, M., Ballhaus, W. F.; and Frick, J. "An Automated Procedure for Computing the Three-Dimensional Transonic Flow Over Wing-Body Combinations, Including Viscous Effects." AFFDL-TR-77-122, Vol. I, February 1978.

[15]Binion, T. W., Jr. "An Investigation of Three-Dimensional Wall Interference in a Variable Porosity Transonic Wind Tunnel." AEDC-TR-74-76, October 1974.

[16]Loving, D. L., and Estabrooks, B. B. "Transonic Wing Investigation in the Langley 8-Foot High-Speed Tunnel at High Subsonic Mach Numbers and at a Mach Number of 1.2." NACA RM L51F07, September 1951.

[17]Treadgold, D. A., Jones, A. F., and Wilson, K. H. "Pressure Distribution Measured in the RAE 8 ft. x 6 ft. Transonic Wind Tunnel on RAE Wing "A" in Combination with an Axi-Symmetric Body at Mach Numbers of 0.4, 0.8, and 0.9." in "Experimental Data Base for Computer Program Assessment." AGARD-AR-138, May 1979.

[18]Newman, P. A., and Allison, D. O. "Comparison of Interference-Free Numerical Results with Sample Experimental Data for the AEDC Wall-Interference Model at Transonic and Subsonic Flow Conditions. NASA TM X-71991, July 1974.

1 Report No	2 Government Accession No	3 Recipient's Catalog No
NASA TM-87707		

4 Title and Subtitle	5 Report Date
UNSTEADY TRANSONIC FLOW CALCULATIONS FOR WING-FUSELAGE CONFIGURATIONS	March 1986
	6 Performing Organization Code 505-63-21-01
7 Author(s)	8 Performing Organization Report No
John T. Batina	
9 Performing Organization Name and Address	10 Work Unit No
NASA Langley Research Center Hampton, VA 23665-5225	11 Contract or Grant No
	13 Type of Report and Period Covered
12 Sponsoring Agency Name and Address	Technical Memorandum
National Aeronautics and Space Administration Washington, DC 20546	14 Sponsoring Agency Code

15 Supplementary Notes

This paper will be presented at the AIAA/ASME/ASCE/AHS 27th Structures, Structural Dynamics and Materials Conference, San Antonio, Texas, May 19-21, 1986 as AIAA Paper No. 86-0862.

16 Abstract

Unsteady transonic flow calculations are presented for wing-fuselage configurations. Calculations are performed by extending the XTRAN3S (Version 1.5) unsteady transonic small-disturbance code to allow the treatment of a fuselage. The research was conducted as part of a larger effort directed toward developing the capability to treat a complete flight vehicle. Details of the XTRAN3S fuselage modeling are discussed in the context of the small-disturbance equation. Transonic calculations are presented for three wing-fuselage configurations with leading edge sweep angles ranging from 0° to 46.76°, the results of which compare well with available experimental steady pressure data. Unsteady calculations are performed for simple bending and torsion modal oscillations of the wing. Comparisons of sectional lift and moment coefficients for the wing-alone and wing-fuselage cases reveal effects of fuselage aerodynamic interference on the unsteady wing loading. Tabulated generalized aerodynamic forces typically used in flutter analyses, indicate small changes in the real (in-phase) component and as much as a 30% change in the imaginary (out-of-phase) component when the fuselage is included in the calculation. These changes result in a ? to 5% increase in total magnitude and a several degree increase in phase.

17 Key Words (Suggested by Author(s))	18 Distribution Statement
Transonic Unsteady Aerodynamics Wing-Fuselage Aerodynamic Interference Aeroelasticity & Flutter	Unclassified - Unlimited Subject Category 02

19 Security Classif (of this report)	20 Security Classif (of this page)	21 No of Pages	22 Price
Unclassified	Unclassified	15	A02

N-305

For sale by the National Technical Information Service, Springfield Virginia 22161

End of Document